Modeling and Control of Industrial ROV's for Semi-Autonomous Subsea Maintenance Services

Mai, Christian; Pedersen, Simon; Hansen, Leif; Jepsen, Kasper Lund; Yang, Zhenyu

Published in:
IFAC-PapersOnLine

DOI (link to publication from Publisher):
10.1016/j.ifacol.2017.08.2535

Publication date:
2017

Document Version
Publisher's PDF, also known as Version of record

Available online at www.sciencedirect.com

ScienceDirect

IFAC Papers Online CONFERENCE PAPER ARCHIVE

IFAC PapersOnLine 50-1 (2017) 13686–13691

Modeling and Control of Industrial ROV's for Semi-Autonomous Subsea Maintenance Services

Christian Mai [**,*] **Simon Pedersen** [*] **Leif Hansen** [*]
Kasper Jepsen [*] **Zhenyu Yang** [*]

[*] *Department of Energy Technology, Aalborg University, Niels Bohrs Vej 8, 6700 Esbjerg, Denmark*
[**] *SDU Mechatronics, University of Southern Denmark, Alsion 2, 6400 Sønderborg, Denmark (E-mail: chrmai@mci.sdu.dk).*

Abstract: Remotely Operated Vechicles (ROV's) takes a big part in the installation, maintenance and inspection of offshore subsea energy activities, such as inspections of Oil & Gas and wind energy pipelines and cables. By improving the ROV automation the operational cost can be significantly decreased as well as improving the inspection quality. This study examines an industrial ROV, where the investigations include modeling of a real industrial prototype, which is then linearized and used for Linear Quadratic Regulator (LQR) development. The results are validated both based on non-linear model simulations. Furthermore, the LQR controller is compared with the existing built-in heading and depth PID controllers, where it is shown that the LQR controller both gives an improved closed-loop transient performance and rejects noise better than the built-in controller. It is concluded that the ROV prototype has an acceptable physical design but that the automation could potentially be improved by adding a MIMO control scheme such as the proposed LQR controller.

Keywords: ROV, modeling, robotics, mechatronics, automation

1. INTRODUCTION & MOTIVATION

Remotely Operated Vehicles (ROV's) are widely used in offshore subsea installations, maintenance and inspection services for pipelines and cables (Reid (2013)). As the offshore industry expands, the cost of ROV's does the same. This is observed in figure 1 from Brun (2014) where both the usage and cost of ROV's are shown. From the figure 1 it is clear that the cost has increased over the last couple of years and it is predicted to increase further in the future. For this reason any decrease in operational cost for the individual ROV can benefit the industry significantly.

ROVs can take many different shapes depending on the objective. Small freely moving underwater ROV's are widely used for minor inspections, where larger ROV's or divers are too expensive. In some of these cases the ROV's tasks can be fully or partly automated to decrease the inspection time and operational cost, see Tena (2011). For this reason the offshore industry is predicted to focus more on the improved automation of the ROV's in the upcoming years, as the potential gain is significantly increasing (Brun (2014)). In this context the fully and semi-automated ROV's, strongly demand precise and fast-tracking control solutions (Evans et al. (2009)), in addition to reliable navigation and positioning system (Paul et al. (2014)). Several different control structures and strategies have been applied in the past, such as PIDs (Rúa and Vásquez (2016)), MPC (Molero et al. (2011)) and LQR (Prasad and Swarup (2015)) based methods, however most small commercial ROVs utilize PID based control.

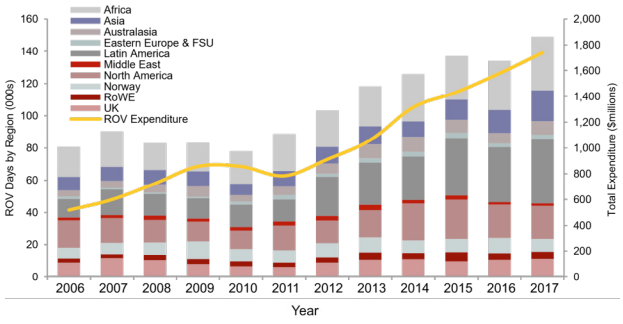

Fig. 1. Historic and prediction data of ROV usage and expenditure. Figure from Brun (2014).

This work will focus on the development of a low-dimensional model for a small industrial ROV prototype, as well as the development of MIMO control strategies, which can improve the precision and speed of the ROV. This ROVs current control solution rely on several manually tuned PID controllers (VideoRay LCC (2012)), and thus a MIMO controller can potentially improve the speed and accuracy of the ROV's position tracking. A detailed controller comparison will be carried out based on non-linear model simulations.

The rest of the paper is organized as follows: In section 2 the considered ROV prototype will be described and the associated modeling will be described in section 3. The controller development and descriptions will be included

10.1016/j.ifacol.2017.08.2535

in section 4, where the control comparison based on the non-linear model simulations will be presented in section 5. Finally, a conclusion will be carried out in section 6.

2. TEST VEHICLE

In this section the considered commercial ROV will be described. The vehicle in question is a VideoRay 4 PRO Rov, which is a small inspection ROV. The vehicle, which is illustrated in fig. 2, weighs $\approx 6.1\,\text{kg}$ and has a size of $375x289x223\,\text{mm}$ with a maximum dive depth of 300m.

Fig. 2. VideoRay 4 Pro ROV

The main components are as follows; a main waterproof electronics chassis, consisting of a front facing camera and inertial measurement unit (a magnetometer, accelerometer, gyro and temperature); two main rear-facing thruster assemblies which provide forward/backward thrust; a ballast skid with adjustable buoyancy; a top assembly which has a plastic buoyancy mass and top mounted up/down thruster.

By default, the sensors are used to calculate the attitude and heading of the vehicle, as well as the depth from sea-surface. The calculated heading and depth are used in the built-in automatic control solution which is described in section 4.2.

3. DYNAMIC MODEL

In this section a 6 degree-of-freedom (6-DOF) model for the ROV will be developed, which will be used for the control design in section 4. The model will describe the linear and angular movements of the vehicle in the coordinate system shown in fig. 3. The motions will be determined by the forces shown in tab. 1, which include force from the thrusters and various internal forces. These forces are illustrated on fig 4

Table 1. Forces on ROV body

Symbol	Description
$F_{(l,t,r)}$	Thruster forces of left, top and right thruster
F_d	Drag force, against
F_g	Gravity force
F_b	Buoyancy force

The main model parameters which will determine the behavior of the ROV are given in table 2.

Table 2. Model parameters

Symbol	Unit	Description
m_t	kg	Mass of ROV
V_t	L	Volume of ROV
D	$\frac{N}{m \cdot s^{-1}}$	Cartesian drag coefficient
B	$\frac{N \cdot m}{rad \cdot s^{-1}}$	Rotational drag coefficient
T	N	Thruster coefficients

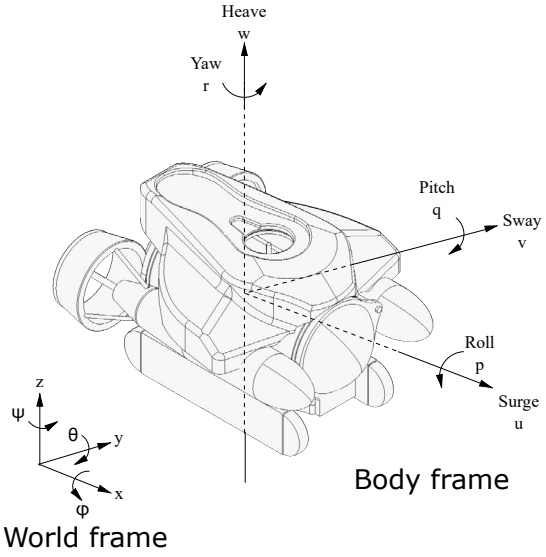

Fig. 3. ROV reference frames

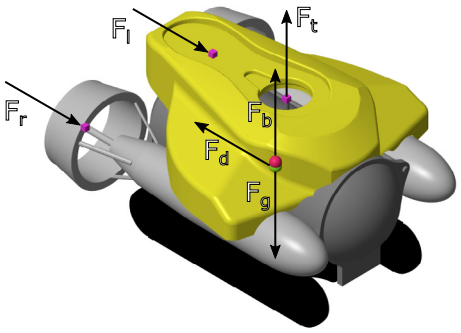

Fig. 4. Visualization of vehicle forces. The purple boxes indicate the points where thruster forces are applied. Red sphere indicates the center of buoyancy (CB), and the green sphere indicates the center of mass (CM)

Buoyancy & Gravity Both the gravity and buoyancy force will act parallel to the z axis in the world frame. Buoyancy is the displacement force of the vehicle, based on the total volume of the vehicle, and can be calculated as shown in (1). Gravity force is calculated using the total mass of the vehicle as shown in (2).

$$F_b = V_t \cdot \rho \cdot g \tag{1}$$
$$F_g = m_t \cdot g \tag{2}$$

where V_t is the total volume, m_t is the total mass, ρ is the density of the liquid, g is the gravitational constant.

Thrusters The thrusters provide actuation force as a function of the control inputs. The thrust force is in principle dependant on two parameters; the propeller

rotation speed, and the advance speed (speed of the propeller through the water), as shown in (3)

$$\hat{F}_t(n, u_a) = \rho D^4 \cdot \left(\alpha_1 + \alpha_2 \cdot \frac{u_a}{n \cdot D}\right) \cdot n|n| \tag{3}$$

Where ρ is the fluid density, D is the propeller diameter, $a_{1,2}$ are the propeller coefficient n is the propeller rotation speed and u_a is the advance speed.

Given a linear relationship between the thruster rotation speed and control input $n = a \cdot u$, and neglecting the influence of the advance speed, the thruster force is modeled as a quadratic equation given the normalized control input u, shown in (4) (Blanke (1981); Wang and Clark (2006)).

$$F_t(u_l, u_t, u_r) = \begin{bmatrix} T_l^l & 0 & 0 \\ 0 & T_l^t & 0 \\ 0 & 0 & T_l^r \end{bmatrix} \cdot \begin{bmatrix} u_l \\ u_t \\ u_r \end{bmatrix} + \begin{bmatrix} T_q^l & 0 & 0 \\ 0 & T_q^t & 0 \\ 0 & 0 & T_q^r \end{bmatrix} \cdot \begin{bmatrix} u_l^2 \\ u_t^2 \\ u_r^2 \end{bmatrix} \tag{4}$$

Where $u_{(l,t,r)}$ are the thruster input signals normalized to ± 1 and T are the thruster coefficients.

Hydrodynamic drag forces The drag forces act against the current velocity of the vehicle, and is applied at the center of mass CM The drag forces on the ROV body are modeled as a quadratic equation as shown in (5) (Blanke (1981); Wang and Clark (2006))

$$F_d(u, v, w) = \begin{bmatrix} D_l^u & 0 & 0 \\ 0 & D_l^v & 0 \\ 0 & 0 & D_l^w \end{bmatrix} \cdot \begin{bmatrix} u \\ v \\ w \end{bmatrix} + \begin{bmatrix} D_q^u & 0 & 0 \\ 0 & D_q^v & 0 \\ 0 & 0 & D_q^w \end{bmatrix} \cdot \begin{bmatrix} u^2 \\ v^2 \\ w^2 \end{bmatrix} \tag{5}$$

where u, w, v are the cartesian velocities, D_l is the linear drag coefficient and D_q is the quadratic drag coefficient

3.1 Determination of coefficients

Body part constants For the body of the ROV, the mass has been found by weighing the individual parts. The volumes of the individual parts and their respective COG's have been found using the CAD model

Table 3. Physical constant for ROV' parts

Name	Mass m_p (kg)	Volume V_p (L)	Offset from chassis CM p_p (mm)
Top	1.18	1.08	$\begin{bmatrix}0 & 0 & -75\end{bmatrix}$
Chassis	1.94	4.10	$\begin{bmatrix}0 & 0 & 0\end{bmatrix}$
Ballast	1.29	0.75	$\begin{bmatrix}0 & 0 & 85\end{bmatrix}$
Left thruster	0.91	0.90	$\begin{bmatrix}0 & -100 & 0\end{bmatrix}$
Right thruster	0.91	0.90	$\begin{bmatrix}0 & 100 & 0\end{bmatrix}$

Drag coefficients The drag coefficients have been derived using coefficients from a previous ROV model (VideoRay Pro 3), which were calculated and verified in Wang and Clark (2006) using strip theory and flume tests.

The drag coefficients for the vehicle used in this work, VideoRay 4, have been recalculated such that the the drag at maximum velocity (VideoRay LCC (2012)) equals the total thruster force as shown in (6). While maintaing the ratio of linear to quadratic drag at the same value as for the VideoRay 3 as shown in (7).

$$F_l(1) + F_r(1) = D_u^q \cdot u_{max}^2 + D_u^l \cdot u_{max} \tag{6}$$

$$\frac{D_u^q}{D_u^l} = C \tag{7}$$

The drag ratio C (scalar relationship between linear and quadratic drag) is calculated given the numbers from Wang and Clark (2006), and is equal to $0.14 - 0.19$ for the three linear axes, with an average of $C = 0.16$.

Using this calculation for the three axes yields the cartesian drag coefficients shown in tab. 4. For the rotational drags, the coefficients from Wang and Clark (2006) have been used directly.

Table 4. Drag coefficients D

Axis	Linear coeff. l	Quadratic coeff. q
u	21.8	3.4
v	110.9	21.2
w	95.1	13.3
p	0.048	0.009
q	0.069	0.012
r	0.450	0.048

Thrust coefficients The thrust coefficients have been derived from the specifications of the thrusters (VideoRay LCC (2012); Wang and Clark (2006)) in a way analogous to the method described above.

Table 5. Thrust coefficients T

Thruster	Linear coeff. l	Quadratic coeff. q
Left/right	32.73	14.40
Top	17.66	3.96

3.2 COM and COB

The centre of mass can be calculated using the operation in (8) due to the fact that the parts are rigidly constrained to each other.

$$\boldsymbol{CM} = \boldsymbol{M_p} \cdot \boldsymbol{p_p} \cdot \frac{1}{m_t} = \begin{bmatrix} 0.00 \\ 0.00 \\ 3.41 \end{bmatrix} (\text{mm}) \tag{8}$$

where $\boldsymbol{M_p}$ is the vector of component masses, p_p is the offset, m_t as is the total mass

Similarly, the centre of buoyancy can be found using the volumes of the bodies as shown in (9).

$$\boldsymbol{CB} = \boldsymbol{V_p} \cdot \boldsymbol{p_p} \cdot \frac{1}{V_t} = \begin{bmatrix} 0.00 \\ 0.00 \\ -2.19 \end{bmatrix} (\text{mm}) \tag{9}$$

where $\boldsymbol{V_p}$ is the vector of component volumes, p_p is the offset, V_t is the total volume.

As can be seen from the results $\boldsymbol{CG}$ and $\boldsymbol{CB}$ the center of gravity and mass are coincident in the $x - y$ axes, whereas there is a difference of 5.59 mm in the z axes. This corresponds well to the self-righting behavior in the roll and pitch directions which the vehicle is designed with.

3.3 Model implementation

The force models described was implemented as a non-linear Simulink™ model using Simscape Multibody™ (formerly SimMechanics™) which provides a multibody simulation environment.

The implemented model consists of the following parts:

- ROV rigid body consisting of 5 parts

- 6-DOF joint between body and world
- (1) Buoyancy force
- (1) Gravity force
- (3) Thruster forces
- (1) Drag forces

The implemented model is illustrated in fig. 5. The thruster force section implements thruster force calculation. The rigid body section implements the rigid body consisting of the 5 ROV parts. The frames and sensing implements the 6-DOF link between the body frame and reference frame, and measures the angular/linear positions and velocities. The buoyancy, gravity and drag forces are implemented in the last section.

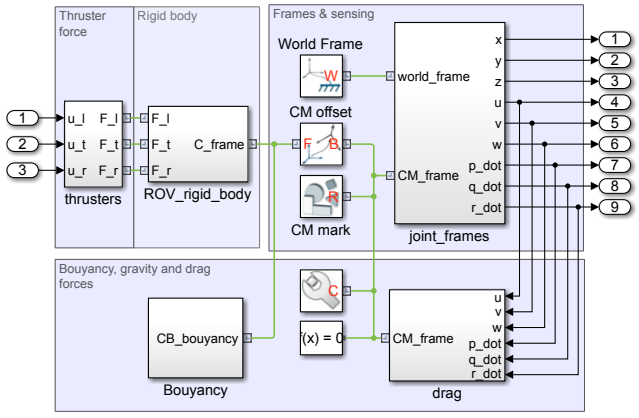

Fig. 5. Simulink-Simscape dynamics model of ROV; green lines mark coordinate systems

3.4 Linearization

A model linearization is carried out for the development of the LQR controller is section 4. The linearization is validated by comparing the linear and non-linear models in step responses for each actuator, respectively.

The model has been linearized by Taylor expansion and thus the Jacobian matrices for a linear state-space model are obtained. The model has the three thrusters as inputs, 12 states $[x, y, z, p, q, r, u, v, w, \dot{p}, \dot{q}, \dot{r}]$ and 6 outputs $[p, q, r, u, v, w]$.

Figure 6 and 7 show the step responses to the angular velocity, and 8 and 9 show the step responses to the linear velocities. The most dominant deviations are the linear velocities, where the non-linear drag force is quadratic and the linearized version is not, which caused large deviation, such that the linear model over-estimates the velocity. Furthermore, the rear-thrusters effect to the y and z and the top-thrusters effect to the x, roll and yaw speed, are neglected in the linearization. In general, the linear and non-linear models behave similarly in the beginning of the simulations (at lower speeds), while the deviation increases over time as expected (when the speed is increased, the quadratic drag effects become more pronounced).

4. CONTROLLER DEVELOPMENT

In this section the development of a Linear Quadratic Regulator (LQR) will be described. The controller is designed on the linearized model with full-state feedback.

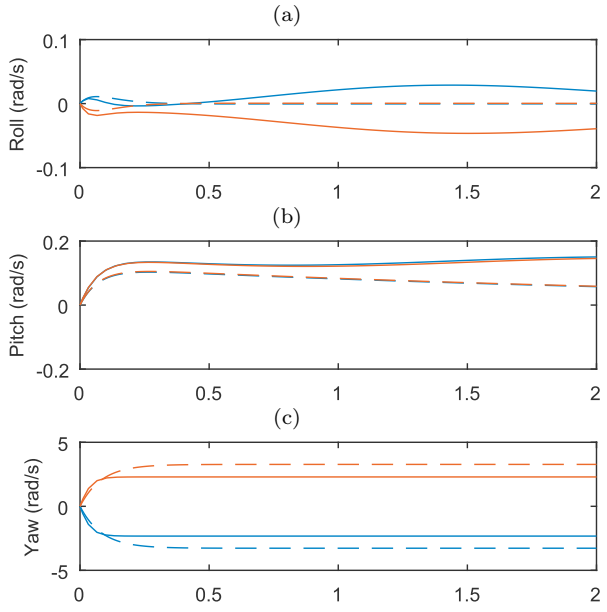

Fig. 6. Angular-velocity step responses to rear-thrusters individually (blue: left thruster, red: right thruster, dashed: linear, full:nonlinear)

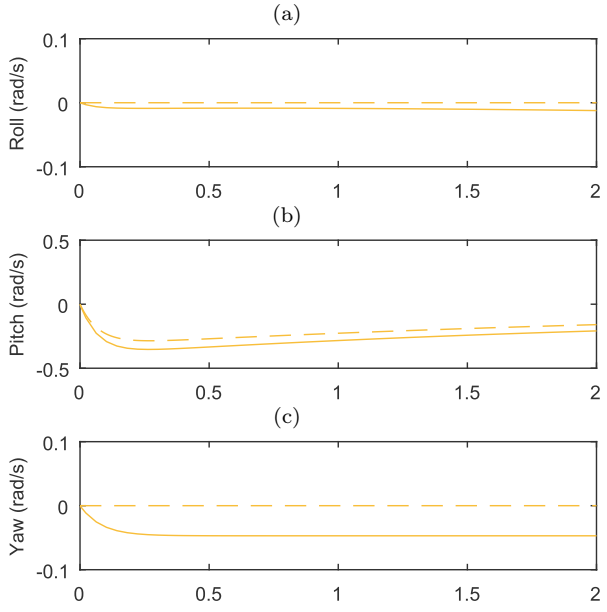

Fig. 7. Angular-velocity step responses to top-thruster (yellow: top thruster)

Additionally, the existing control solution which is based on PIDs will be described.

4.1 Controlability and observability

The linearized models controllability is analyzed, and it is shown that it is uncontrollable for the states $\mathbf{v}$ and $\mathbf{y}$, as

$$length(A) - rank(Co) = 2 \tag{10}$$

where

$$Co = \begin{bmatrix} B & AB & A^2B & \dots & A^{n-1}B \end{bmatrix} \tag{11}$$

However, the model is still stabilizable, and hence the state can be neglected in the control strategy. It has to be noted that the non-linear model has some relationship

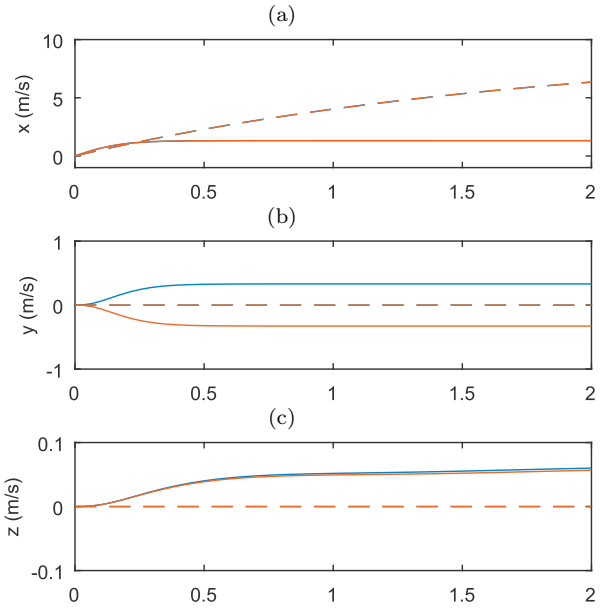

Fig. 8. Linear-velocity responses to rear-thrusters individually (blue: left thruster, red: right thruster)

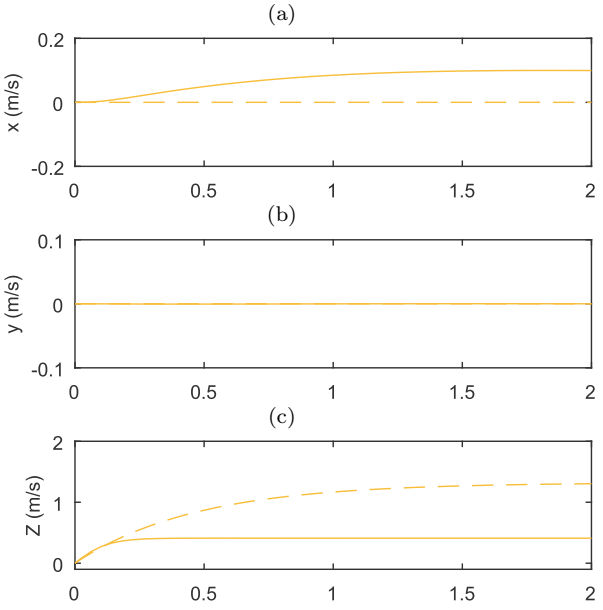

Fig. 9. Linear-velocity step responses to top-thruster (yellow: top thruster)

between the inputs and v, which is then linearized away. As v and y are uncontrollable in the original model, minimum realization is applied to remove these outputs (such that they can be neglected for control development).

Full-state feedback is required for the considered LQR control design. Thus, all model states have to either directly measured or observed. The model is observable as

$$length(A) - rank(Ob) = 0 \tag{12}$$

where

$$Ob = \begin{bmatrix} C & CA & CA^2 & .. & CA^{n-1} \end{bmatrix}^T \tag{13}$$

This was also expected, as the p, q and r can be estimated from $\dot{p}$, $\dot{q}$ and $\dot{r}$ directly, respectively.

4.2 Existing built-in controller

The existing built-in control solutions are structured as two independent ideal PID control loops controlling the following motions:

- Heading, measured by compass $\left[P = 3.44 \cdot 10^{-2}, I = 2.29 \cdot 10^{-3}, D = 0.458\right]$
- Depth, measured by barometric pressure $\left[P = 2 \cdot 10^{-2}, I = 4 \cdot 10^{-3}, D = 0\right]$

The heading is controlled by the F_l and F_r with opposite sign, and the depth is controlled by F_t. However, these controllers do not take into account the cross coupling of forward/back motion and up/down motion as shown in the model. Therefore there exists the potential for significant improvement of control performance by introducing an intelligent MIMO control scheme, which will be developed in the following section.

4.3 Optimal controller

A standard LQR controller is designed for the linearized ROV model. It is a standard optimization problem, where the cost function, J, is minimized by changing the state-feedback controller, K. The cost function is

$$J = \int_0^\infty (x^T Q x + u^T R u) dt \tag{14}$$

Q and R are tuned based on Bryson's rule (Bryson and Ho (1969)), that states

$$Q_{ii} = 1/maximum\ acceptable\ value\ of\ \left[x_i^2\right] \tag{15}$$

$$R_{ii} = 1/maximum\ acceptable\ value\ of\ \left[u_i^2\right] \tag{16}$$

here R_{ii} is weighted according to the saturation values of u_i, and Q_{ii} is designed such that p, q and r and their derivatives, are weighted dominant over u and w.

5. CONTROL SIMULATION RESULTS

In this section the simulation results will be examined. For completeness, the comparison will be based on simulations with the non-linear model. The examination will also be based on a control comparison between the built-in PID controllers and the new LQR controller.

The comparison will be based on step responses of the heading and depth setpoints, as the built-in PID controllers only are designed for tracking these two references. Specifically, the controller comparison will examine a case where the ROV aims to move 1 m in the z position and $\frac{pi}{2}$ rad in the yaw angle.

Figure 10 shows the position responses, where the setpoint for z is stepped at $t = 0$. It is clear that both controllers track the setpoint satisfyingly with a fast settling time and minimal steady-state error. However, for the PID controller, the x position will increasingly diverge from zero and the y position will stabilize away from zero, as the PID controller does not consider multiple setpoints. The LQR controller on the other hand keeps all positions close to the respective setpoints.

Figure 11 p, q and r positions, where the setpoint for r is stepped at $t = 0$. Here, the PID controller is faster

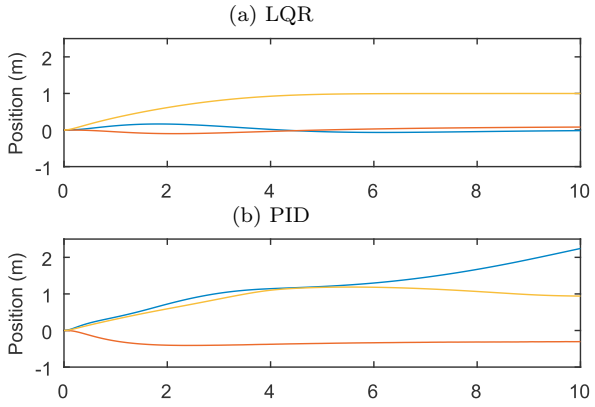

Fig. 10. Controller comparison. Linear-position responses: x is blue, y is red, z is yellow

than the LQR controller. This is mainly due to the fact that these outputs were weighted smaller in the Q matrix for the LQR controller. However, it is clear that the two controller perform similarly and no big difference can be observed.

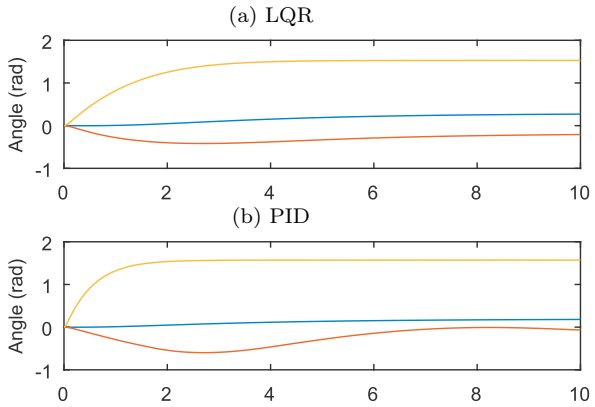

Fig. 11. Controller comparison. Angle-position responses: p is blue, q is red, r is yellow

In general the results show that the position controller for z is acceptable for both controllers, however the PID controller does not consider the deviation of the other positions x and y, which clearly limits the usability of the controller in practical cases. The angle controllers perform similarly, although the PID controller is a little faster than the LQR controller. It was also observed during simulations that if noise was added to the measurements, the heading PID controller performed significantly worse (larger deviation and repeated saturation of the actuators) due to the high derivative control gain. If the noise was filtered, the derivative gain was less detrimental, but this also correspondingly reduced the speed of the controller.

6. CONCLUSION AND FUTURE WORK

This study has examined an industrial underwater ROV designed for subsea inspection and maintenance tasks. First, a physical description has been made, and then the ROV modeling has been carried out with a combination of first principle modeling equations and a verified Simscape model.

The linearized model has been analyzed, where it has been shown that the open-loop system is fully observable, but uncontrollable for sway (noted as v) and heave (noted as z). For this reason a minimum realization have been carried out, and the updated model is used for a full-state feedback LQR control scheme.

The obtained LQR controller is compared with the two built-in PID controllers for the heading and depth. The comparison is based on simulations with the non-linear model, and it is clearly shown that the LQR controller is faster, but also that it is much better at keeping the other outputs close to zero. Furthermore, the LQR controller is less sensitive to noise as the heading PID controller has a significant derivative gain.

The overall conclusion is that the considered ROV's prototype design is compact, handy and maneuverable, but also that the built-in controller potentially can be improved by introducing a fast MIMO controller. In future work the designed controller will be implemented on the real ROV, to verify the promising simulation results.

REFERENCES

Blanke, M. (1981). Ship Propulsion Losses Related to Automated Steering and Prime Mover Control. *PhD thesis, The Technical University of Denmark, Lyngby.*

Brun, L. (2014). ROV/AUV Trends: Market and Technology.

Bryson, A.E. and Ho, Y.C. (1969). Applied Optimal Control.

Evans, J., Patron, P., Privat, B., Johnson, N., and Capus, C. (2009). AUTOTRACKER: Autonomous Inspection - Capabilities and Lessons Learned in Offshore Operations.

Molero, a., Dunia, R., Cappelletto, J., and Fernandez, G. (2011). Model predictive control of remotely operated underwater vehicles. *IEEE Conference on Decision and Control and European Control Conference*, 2058–2063. doi:10.1109/CDC.2011.6161447.

Paul, L., Saeedi, S., Seto, M., and Li, H. (2014). AUV Navigation and Localization: A Review.

Prasad, M.P.R. and Swarup, A. (2015). Position and Velocity control of Remotely Operated Underwater Vehicle using Model Predictive Control. *Indian Journal of Geo-Marine Sciences*, 44(12), 1920–1927.

Reid, A. (2013). ROV Market Prospects. URL `http://www.subseauk.com/documents/presentations/ssuk%20-%20rov%20event%20-%20sep%202013%20%5Bweb%5D.pdf`.

Rúa, S. and Vásquez, R.E. (2016). Development of a Low-Level Control System for the ROV Visor3. *International Journal of Navigation and Observation*, 2016, 1–12. doi:10.1155/2016/8029124. URL `http://www.hindawi.com/journals/ijno/2016/8029124/`.

Tena, I. (2011). Automating ROV Operations in aid of the Oil & Gas Offshore Industry.

VideoRay LCC (2012). VideoRay Pro 4 Operator Manual. URL `http://download.videoray.com/documentation/v1_7_0/pdf/pro4/pro4_user_doc_v1_7_0.pdf`.

Wang, W. and Clark, C.M. (2006). Modeling and Simulation of the VideoRay Pro III Underwater Vehicle. *IEEE OCEANS 2006.*